2nd International Congress on 3D Materials Science
Edited by: Dominique Bernard, Jean-Yves Buffière, Tresa Pollock, Henning Friis Poulsen, Anthony Rollett, and Michael Uchic
TMS (The Minerals, Metals & Materials Society), 2014

3D STOCHASTIC MODELING OF MICROSTRUCTURE EVOLUTION DURING THE SOLIDIFICATION OF DENDRITIC ALLOYS

L. Nastac and D. Zhang

The University of Alabama, Department of Metallurgical and Materials Engineering,
Box 870202, Tuscaloosa, AL, 35487, USA, email: lnastac@eng.ua.edu

Keywords: 3D stochastic mesoscopic modeling; Casting; Solidification processing; Dendritic microstructure evolution

Abstract

A comprehensive three-dimensional (3D) stochastic model for simulating the evolution of dendritic crystals during the solidification of binary alloys was developed. The model includes time-dependent computations for temperature distribution, solute redistribution in the liquid and solid phases, curvature, and growth anisotropy. 3D mesoscopic computations at the dendrite tip length scale were performed to simulate the evolution of columnar and equiaxed dendritic morphologies and compared then with predictions obtained with 2D mesoscopic computations.

Introduction

A two-dimensional (2D) stochastic model was developed for the modelling of the evolution of dendritic morphologies during solidification [l]. Favorable comparison of predictions with measured microstructures requires the 2D stochastic model to be extended to 3D. Several 3D models for simulating dendritic growth have been proposed in the literature including phase field approach [2, 3] and Lattice Boltzmann and Cellular Automaton approach [4]. To be efficient, these models require parallel computations and can be used only for relatively small domains. A 3D Cellular Automaton approach for modeling the evolution of dendritic grains has also been developed [5]. This 3D dendritic grain model is relatively fast but it cannot simulate the evolution of dendrites and of microsegregation patterns at the dendrite tip level. Thus, main goal of the current contribution is to develop an efficient 3D stochastic mesoscale dendritic growth model based on the previously developed 2D stochastic mesoscale dendritic growth model presented in [1]. Comparisons of 2D and the 3D predictions in terms of microstructure evolution are also provided.

Stochastic Dendritic Solidification Model

The mathematical representation of the dendritic solidification process of a binary alloy is considered in a restricted 3-D domain ($\boldsymbol{\Omega}$). A cross section of this 3D domain is shown in Fig. 1. Here, $\vec{n}$ is the interface normal vector, $\overline{K}$ is the mean curvature of the interface, and the curve $\boldsymbol{\Gamma}$ represents the solid/liquid (S/L) interface which evolves in time and has to be found as part of the solution. The solidification of binary alloys is governed by the evolution of the temperature ($T(x,y,z,t)$) and concentration ($C(x,y,z,t)$) fields that have to satisfy several boundary conditions at the moving S/L interface as well as the imposed initial and boundary conditions on the computational domain. The equations that describe the physics of the solidification process in 3-D Cartesian coordinates are as follows (see the 2D equations in [1, 6-8]).

- Temperature (T) in $\boldsymbol{\Omega}$ (heat transfer equation):

$$\rho\, c_p \frac{\partial T}{\partial t} = \frac{\partial}{\partial x}\left(K \frac{\partial T}{\partial x} \right) + \frac{\partial}{\partial y}\left(K \frac{\partial T}{\partial y} \right) + \frac{\partial}{\partial z}\left(K \frac{\partial T}{\partial z} \right) - \rho\, L \frac{\partial f_L}{\partial t} \text{ with } f_L = 1 - f_S \quad (1)$$

where t is time, ρ is the density, K is the thermal conductivity, c_p is the specific heat, L is the latent heat of solidification, f_L is the liquid fraction, f_S is the solid fraction, and x, y and z are the domain coordinates.

- Concentration (C) in $\boldsymbol{\Omega}$ (solute diffusion equation):

In the liquid phase (C_L): $$\frac{\partial C_L}{\partial t} = \frac{\partial}{\partial x}\left(D_L \frac{\partial C_L}{\partial x} \right) + \frac{\partial}{\partial y}\left(D_L \frac{\partial C_L}{\partial y} \right) + \frac{\partial}{\partial z}\left(D_L \frac{\partial C_L}{\partial z} \right) \quad (2)$$

In the solid phase (C_S): $$\frac{\partial C_S}{\partial t} = \frac{\partial}{\partial x}\left(D_S \frac{\partial C_S}{\partial x} \right) + \frac{\partial}{\partial y}\left(D_S \frac{\partial C_S}{\partial y} \right) + \frac{\partial}{\partial z}\left(D_S \frac{\partial C_S}{\partial z} \right) \quad (3)$$

where D_L and D_S are the interdiffusion coefficients in the liquid and solid, respectively.

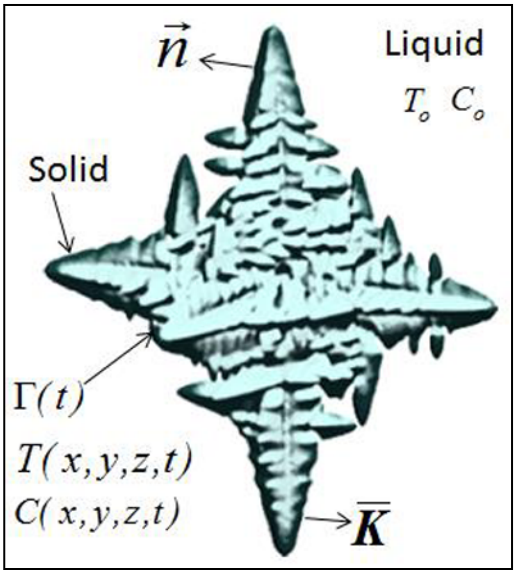

Figure 1. A 3D-domain for dendritic solidification.

Local equilibrium at the S/L interface on $\Gamma(t)$ (here, "*" means at interface):

$$C_S^* = k\, C_L^* \quad (4)$$

- Solute conservation at the S/L interface:

$$V_n^*\, C_L^* \left(k - 1\right) = \left(- D_L \left(\frac{\partial C_L}{\partial x} + \frac{\partial C_L}{\partial y} + \frac{\partial C_L}{\partial z} \right) + D_S \left(\frac{\partial C_S}{\partial x} + \frac{\partial C_S}{\partial y} + \frac{\partial C_S}{\partial z} \right) \right) \cdot \vec{n} \quad (5)$$

where V_n^* is the normal velocity of the interface and $\vec{n}$ denotes the normal to the S/L interface that is pointing into the liquid (see Fig. 1).

- The interface temperature (T^*) is defined as (assuming local equilibrium with both phases):

$$T^* = T_L^{EQ} + \left(C_L^* - C_0\right) m_L - \Gamma\, \overline{K}\; f(\varphi, \theta) \quad (6)$$

where T_L^{EQ} is the equilibrium liquidus temperature of the alloy, m_L is the liquidus slope, $\overline{\boldsymbol{K}}$ is the mean curvature of the S/L interface, Γ is the Gibbs-Thomson coefficient, and $f(\varphi,\theta)$ is a coefficient that accounts for growth anisotropy, where φ is the growth angle (*i.e.*, the angle between the normal and the growth axis) and θ is the crystallographic orientation angle.

In Eq. (6), second term in the right side is the constitutional undercooling and the last term in the right side is the curvature undercooling (that reduces the total undercooling at the dendrite tip, that is, has a stabilizing effect on the S/L interface). The interface temperature is also affected by the kinetic undercooling. The kinetic undercooling is not accounted for in this model since its effect becomes significant only at very high solidification velocities (*i.e.*, in the rapid solidification regime). Also, the coefficient $f(\varphi,\theta)$ in Equation (6) assumes an axisymmetric approximation where the anisotropy and the interface shape are independent of the polar angle ϕ in the *x-y* plane perpendicular to the growth axis [2].

The solidification process is governed by Eqs. (1) to (6) and a stochastic model for nucleation and growth. The numerical procedures for calculating the nucleation and growth, temperature and concentration fields as well as the growth velocity of the S/L interface are described in details in [9]. It consists of a regular network of cells that resembles the geometry of interest. The model is characterized by (a) geometry of the cell; (b) state of the cell; (c) neighborhood configuration; and (d) several transition rules that determine the state of the cell. In this work, the geometry of the cell is a cube. Each cell has three possible states: "liquid", "interface", or "solid". The selected neighborhood configuration is based on the cubic von Neumann's definition of neighborhood, that is the first order configuration and it contains the first six nearest neighbors. Solidification behavior depends to a great extent on the transition rules. In this model, the change of state of the cells from "liquid" to "interface" to "solid" is initiated either by nucleation or by growth of the dendrites.

An explicit finite difference scheme is used for calculating the concentration fields in the liquid and solid phases. Zero-flux boundary conditions were used for cells located at the surface of the geometry. The solution algorithm includes the "interface" cells by multiplying the concentration in the liquid by the liquid fraction and the concentration in the solid by the solid fraction of the particular interface cell. Also, during each time-step calculation and for each "interface" cell, the previous values of the liquid and solid concentrations are updated to the current values of the interface liquid and solid concentrations calculated with Eqs. (4), (5) and (7). The calculation of the interface liquid concentration, C_L^* can be obtained from Eq. (6) as

$$C_L^* = C_O + \frac{\left(T^* - T_L^{EQ} + \Gamma\,\overline{K}\,f(\varphi,\theta)\right)}{m_L} \tag{7}$$

The procedures for calculating $\overline{K}$ and $f(\varphi,\theta)$ are described below.

The average interface curvature for a cell with the solid fraction f_S is calculated with the following expression:

$$\overline{K} = \frac{1}{a}\left(1 - 2\,\frac{f_S + \sum_{k=1}^{N} f_S(k)}{N+1}\right) \tag{8}$$

where N is the number of neighboring cells. In the present 3D calculations, $N = 26$, that contains all the first order neighboring cells (including the diagonal cells). Equation (8) is a simple counting-cell technique that approximates the mean geometrical curvature (and not the local geometrical curvature). An improved curvature model is presented in [8]. A comparison of 2D simulations obtained with these curvature models was also provided in [8].

The anisotropy of the surface tension (see Eq. (6)) is calculated as [2]:

$$f(\varphi,\theta)=1+\frac{4\delta}{1-3\delta}\left(\cos^4(\varphi-\theta)+\frac{3}{4}\sin^4(\varphi-\theta)\right) \quad \text{with } \varphi=a\cos\left(\frac{V_z}{\left[(V_x)^2+(V_y)^2+(V_z)^2\right]^{1/2}}\right) \quad (9)$$

where φ is the angle between the normal direction to the solid-liquid interface and the [100] direction (growth axis), V is computed with Eq. [12] in [10], θ is calculated with Eq. (7) in [10] and δ accounts for the degree of anisotropy. For cubic symmetry, $\delta = 0.047$ [2].

The algorithm is presented in [10]. The simulation software was written in Visual Fortran 90. The output of the model consists of screen plotting at any chosen time of *C*, *T*, or color indexes of all cells. Also, the final values of *C*, *T*, and color indexes of all cells are saved at the end of computations on the computer disk.

Results and Discussion

Thermo-physical properties of the alloys used in simulations are presented in Table 1. The dimensions of the 2D and 3D simulation domains are 2 mm x 4 mm and 2 mm x 4 mm x 1 mm, respectively. The grid size is fine enough to approximately resolve the dendrite tip radius under the current solidification conditions. Newton cooling boundary condition was applied only to the bottom of the computational domain. All other boundaries were perfectly insulated.

The surface heat transfer coefficient used in the present simulations is $h = 10^3$ W m^{-2} K^{-1}. Zero-flux solute boundary conditions were applied at the boundaries of the computational domain (*i.e.*, a closed system was assumed). The initial melt temperature was 1400 °C. Also, an initial concentration equal to C_o was assumed everywhere on the computational domain.

Table 1. Thermophysical properties of IN718-5Nb used in simulations [9, 11].

Property	μ_N^C [m^{-2} K^{-2}]	μ_N^E [m^{-3} K^{-2}]	L [J/kg]	ρ [kg/m^3]	K [W/m/K]	c_p [J/kg/K]	T$_L$ [°C]
Value	1x10^6	5x10^8	2.9x10^5	7620	30.1	720	1336
Property	C_o [wt.%]	C_{eut} [wt.%]	k_o -	D_L [m^2 s^{-1}]	D_S [m^2 s^{-1}]	m_L [°C %$^{-1}$]	Γ [K m]
Value	5.0	19.1	0.48	3x10^{-9}	1x10^{-12}	-10.5	3.65x10^{-7}

In Fig. 2, a comparison of 2D (a) and 3D (b) simulated microstructures (columnar dendritic morphologies) in unidirectional solidification of IN718-5 wt. % Nb alloy is presented. The 2D computations were done by using the 2D stochastic dendritic model presented in [1, 6-8]. The 3D simulation results are taken from the middle of the simulated sample (x-y plane with z = 0.5 mm). The competition between nucleation and growth of multiple columnar dendrites is evident in both 2D and 3D cases. The strong growth competition from the sample bottom (>20 dendrites) to 1/4 of the sample height (10 dendrites) to 1/2 of the sample height (5 dendrites in 2D and 7 dendrites in 3D) to 3/4 of the sample height (3 dendrites in 2D and 4 dendrites in 3D) can be observed. For 3D computations, more dendrites are observed toward the top of the sample because more nucleation sites are available in 3D than in 2D and also because some dendrites that are visualized are cut from a different plane. Note also that the columnar morphologies look different in 3D than in 2D.

Figure 3 shows a comparison between 2D and 3D computations in terms of equiaxed dendritic morphologies. The legend in Figs. 2 and 3 shows the 256 color indexes (*CI*, illustrated here in 16 classes, where each class contains 16 different color indexes) that is used for displaying the preferential crystallographic orientation angle.

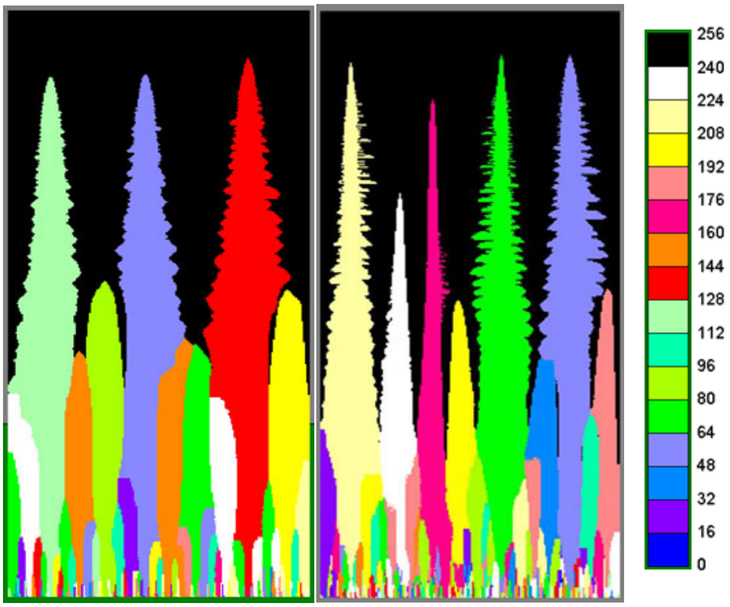

(a) (b) *CI*

Figure 2. Comparison of 2D (a) and 3D (b) simulated microstructures (columnar dendritic morphologies) in unidirectional solidification of IN718-5 wt.% Nb alloy.

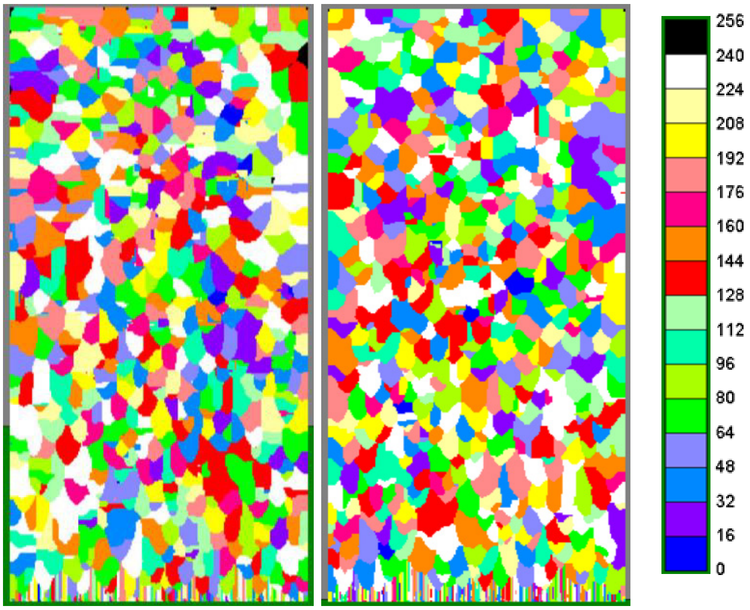

(a) (b) *CI*

Figure 3. Comparison of 2D (a) and 3D (b) simulated microstructures (equiaxed dendritic morphologies) in unidirectional solidification of IN718-5 wt.% Nb alloy

The orientation angles (θ) can be extracted from the legend in Figs, 2 and 3 by using the following equation: $\theta = \pi/2*(CI/255)-\pi/4$. Thus, when $CI/255$ varies from 0 to 1, θ ranges from $-\pi/4$to $\pi/4$.

The equiaxed grain density was fx10^8 nuclei/m^2 in 2D and 10^{12} nuclei/m^2 in 3D. The conversion factor $f = \pi/4$ [12]. Similar equiaxed morphologies can be observed from Fig. 3 for both 2D and 3D cases, implying that 2D computations can be used and then the grain size can be converted to 3D by using the “1/f” conversion factor.

A RAM memory size of 100 bytes/cell is needed in the present 3D computations. CPU-time is related to the domain size and the time-step and, for the simulation problems presented in Figs. 2 and 3, is of the order of few hours on a Dell Precision T7500 desktop.

Conclusions

An efficient 3D mesoscale stochastic model was developed. The model was applied to simulate 3D microstructures using PCs with reasonable amount of RAM and CPU time and therefore no parallel computations were needed.

It was observed that the 3D columnar dendritic morphologies look different than the 2D columnar dendritic morphologies. This is due to the fact that, for a 2D geometry, the grain growth is constrained in the x-y plane while for the 3D case it is free in the third (z) direction.

Nevertheless, the predicted 3D equiaxed dendritic morphologies look similar to the 2D equiaxed dendritic morphologies. A simple conversion factor ($4/\pi$) can be used to convert the 2D grain size to 3D grain size.

References

1. L. Nastac, *Acta Materialia*, Vol. 47, No. 17, pp. 4253-4262, 1999.
2. A. Karma and W. J. Rappel, *Phys. Rev. E*, vol. 57, No. 4, pp. 4323–4349, 1998.
3. J. H. Jeong,, N. Goldenfeld, and J. A. Dantzig, *Phys. Rev. E*, vol. 64, 041602. pp. 1-14, 2001.
4. M. Eshragi, S. D. Felicelli, and B. Jelinek, Journal of Crystal growth, vol. 354, issue 1, pp. 129–134, 2012.
5. C. A. Gandin, and M. Rappaz, Acta Met. Vol. 45, No. 5, pp. 2187-2195, 1997.
6. L. Nastac, *4th Pacific Rim International Conference on Modeling of Casting and Solidification Processes (MCSP-4)*, Ed. C. P. Hong, Yonsei University, Seoul, Korea, September 5-8, 1999.
7. L. Nastac, Proceedings of the *"Modelling of Casting, Welding, and Advanced Solidification Processes IX"*, Engineering Foundation, Aachen, Germany, August 20-25, 2000.
8. L. Nastac, Modeling and Simulation of Microstructure Evolution in Solidifying Alloys Springer, New York, 2004 (ISBN 978-1-4020-7831-6).
9. L. Nastac and D. M. Stefanescu, *Modelling and Simulation in Materials Science and Engineering*, *Institute of Physics Publishing*, Vol. 5, No. 4, pp. 391-420, 1997.
10. L. Nastac, A 3-D Stochastic Mesoscopic Model for Prediction of Microstructure Evolution during Solidification of Dendritic Alloys, accepted for publication in the journal of *Metallurgical Research & Technology*, EDP Sciences, March 20, 2014.
11. L. Nastac and D. M. Stefanescu, *Metallurgical Transactions*, Vol. 28A, pp. 1582-1587, 1997.
12. M. Kong, R. N. Bhattacharyal, C. James and A. Basu, Geological Society of America Bulletin, vol. 117, no 1-2, pp. 244-249, 2005.